



33 1. Introduction

34 Large and damaging tsunamis are commonly triggered by megathrust ruptures that occur
35 along convergent plate boundaries (i.e. Subduction zones). Since 1900, many megathrust
36 ruptures have triggered numerous devastating near- and far-field tsunamis including the
37 1952 M_w 8.8-9.0 Kamchatka (e.g., Johnson & Satake 1999; Kanamori 1976), the 1960 M_w 9.5
38 in the Chile subduction (e.g., Cifuentes 1989; Moreno et al. 2009), the 1964 M_w 9.2 Alaska
39 (e.g., Plafker 1965), the 2004 M_w 9.2 Sumatra-Andaman Earthquake along northern Sunda
40 Trench (e.g., Vigny et al. 2005; Banerjee et al. 2007; Chlieh et al. 2007) , and the more
41 recent 2010 M_w 8.8 Maule in Chile (e.g., Vigny et al. 2011; Pollitz et al. 2011) and 2011 M_w
42 9.0 Tohoku-Oki earthquake along the northwest border of the pacific ocean (e.g., Koketsu
43 et al. 2011; Wei et al. 2012). These earthquakes and their associated subduction zones
44 have been intensively studied from different perspectives, including their tectonic settings
45 and long-term evolution, seismic activities, geodetic and geophysical features. In contrast,
46 the Manila subduction zone (MSZ), which extends from the southern Taiwan to the
47 southern tip of the Luzon Island in Philippines along the eastern margin of the South China
48 Sea (SCS) (Figure 1), receives less attention, even though it shares many similarities with
49 megathrust systems where large tsunamigenic earthquakes have occurred (Hsu et al.,
50 2012, 2016).

51

52 Over the past decade, attempts to study megathrust earthquakes and tsunamis from the
53 Manila subduction zone are starting to gain momentum. A number of rupture models have
54 been used to assess potential tsunami hazard in the SCS (e.g., Hong Nguyen et al., 2014; Liu
55 et al., 2009; Megawati et al., 2009; Okal et al., 2011; Wu and Huang, 2009) and yet, the
56 simulated tsunami wave heights and the subsequent hazard assessments are considerably
57 inconsistent (Hong Nguyen et al., 2014; Liu et al., 2009; Megawati et al., 2009; Okal et al.,
58 2011; Wu and Huang, 2009; Xie et al., 2019). The difference often lies in the proposed fault-
59 slip magnitudes of these models, and also the fault geometries used. Large variability in the
60 results produced by these models underscores the fact that the seismogenic behaviors of
61 the MSZ are still poorly understood. Some of the challenges which stand out and need to be
62 resolved include assessing whether the MSZ is capable of hosting M_9+ earthquakes; and
63 investigating the amount of tectonic strain it has accumulated, its style of strain
64 accumulation and constraining how that strain is likely to be released in future.



65

66 Several lines of evidence suggest that the Manila trench has the potential to host a giant
67 rupture capable of generating a basin wide tsunami. Firstly, both historical earthquake
68 records and modern seismicity databases (Hsu et al., 2012, 2016) indicate an absence of
69 earthquakes larger than M_w 7.6 since Spanish colonization of Luzon in 1560s (Bautista et al.,
70 2012; Megawati et al., 2009; Ramos et al., 2017; Terry et al., 2017). The lack of significant
71 megathrust-related earthquakes in modern records implies that either a predominately
72 aseismic megathrust or a highly coupled interseismic megathrust with the potential for a
73 large (M_w 8.5+) rupture (e.g. Hsu et al. 2012) is likely to occur. Several recent studies favor
74 the high interseismic coupling model, since both the analysis of earthquake focal
75 mechanisms and geodetic monitoring results demonstrate that the upper plate is under
76 shortening, which suggests that the megathrust, at least since 1960s, shows minimal
77 creeping (Bautista et al., 2001; Hsu et al., 2012, 2016). Secondly, the rate of plate
78 convergence across the Manila trench is up to 90-100 mm/year- faster than the
79 convergence rate of the Sumatra, Japan and Nankai subduction zones, all of which have
80 hosted giant earthquakes in the past few decades (McCaffrey, 2008; Megawati et al., 2009;
81 Hsu et al., 2016, 2012;). Since the MSZ did not produce any significant events in the past
82 four centuries, >30m of slip deficit is estimated to have been accumulated on the
83 subducting interface (Megawati et al., 2009; Hsu et al., 2016). Thirdly, historical
84 documents together with a few geological records across the SCS basin have reported
85 nearly 130 tsunami-events with different generation mechanisms (i.e. Earthquakes,
86 submarine landslides, volcanic eruptions). Although the credibility levels of these records
87 varies (Bautista et al., 2012; Lau et al., 2010; Paris et al., 2014) and the geological-based
88 interpretation suffers from the challenges of distinguishing tsunami waves from extreme
89 storm surges, a series of records stand out with similar range of event ages. Notably, four
90 independent geological and geomorphological studies (Ramos et al., 2017; Sun et al., 2013;
91 Yang et al., 2018; Yu et al., 2009) (Figure 1) have purported evidence from coastal deposits
92 which they have inferred to be the result of large tsunami event in SCS around 1000 to
93 1064 A.D., which is of near coincidence with a historical large wave event recorded in
94 Chaoan, Guangdong in November, 1076 A.D. (Lau et al., 2010). The four independent sites
95 of geological evidence are located at Dongdao island (Sun et al. 2013), Yongshu island (Yu
96 et al., 2009), Badoc island near Luzon (Ramos et al., 2017) and Nanao island in southern



97 Chinese coastline (Yang et al., 2018) (Figure 1). Since these studies identified only one
98 event and if it were indeed generated by one tsunami, then we can conclude that the event
99 was likely to be basin-wide and could only have been triggered by a very large MSZ event.
100 Such an event will be a megathrust earthquake with sufficiently large rupture up to 1,000
101 km long. Such a long and persistent rupture is comparable to the rupture length of the
102 2004 Sumatra-Andaman earthquake (e.g. Megawati et al., 2009). With the afore-mentioned
103 pieces of evidence, there is no reason to rule out the possibility that the Manila trench could
104 rupture as an M_w 9 earthquake (i.e. Megawati et al. 2009; Hsu et al. 2016). The current
105 status of the Manila subduction zone could be an analog of the Sumatran subduction zone
106 before the 2004 M_w 9.2 Sumatra-Andaman event between Myanmar and Aceh where a
107 paucity of earthquake $> M_w$ 8 precede the 2004 event (Chlieh et al., 2008; Hsu et al., 2012),
108 despite of the very different geological settings (i.e. age, buoyancy, fault geometry) between
109 these two subduction zones.

110

111 The SCS region is vulnerable to potential tsunami hazard. It covers an area ca.3.5 million
112 km² (Terry et al., 2017), and is encircled by the coastlines of southeastern China, southern
113 Taiwan, western Philippines, eastern Vietnam, northern Borneo and eastern Malaysia,
114 forming a semi-enclosed basin (Figure 1). The SCS coastline is one of the world's most
115 densely populated with more than 80 million people living in the surrounding coastal cities
116 (Terry et al., 2017). Many of these coastal cities serve as the economic centers and play
117 pivotal roles in their respective countries' economic development. The coastline also hosts
118 a very high density of major infrastructure (i.e. nuclear power plants, ports, airports). Data
119 from the World Nuclear Association shows that more than 10 nuclear power plants are
120 currently in operation or about to start construction in the SCS coastline
121 (<http://www.world-nuclear.org/information-library>). Thus, if a large megathrust
122 earthquake (e.g. $M_w > 9$) were to occur within the SCS basin (Li et al., 2018), the impact
123 would be amplified and much more devastating as the SCS is only ca.1/20 the size of the
124 Indian Ocean. It is therefore crucial to provide physical-based earthquake rupture models
125 for a more realistic tsunami hazard assessment in the SCS region.

126

127 This study differs from previous studies (e.g., Hong Nguyen et al., 2014; Liu et al., 2009;
128 Megawati et al., 2009; Okal et al., 2011; Wu and Huang, 2009), because we utilize the



129 geodetic coupling model constrained by 17 years of GPS velocity measurements (Hsu et al.,
130 2016) to propose a suite of better constrained physically based earthquake rupture
131 scenarios. We also consider rupture segmentations constrained by the geological
132 characteristics and the relief of the subducting Sunda plate. Our rupture models afford
133 standard examples for an improved understanding of the tsunami hazard in the SCS. As a
134 demonstration, we implement the rupture models to conduct hydrodynamic simulations to
135 assess the tsunami characteristics along the coastlines of the SCS.
136

137 **2. Refined possible rupture scenarios**

138 Forecasting the extent and the slip distribution of earthquake ruptures is a challenging task.
139 Before the 2004 M_w 9.2 Sumatra-Andaman earthquake (Chlieh et al., 2008), an M_w 9
140 earthquake had never been anticipated along the Sunda Trench, due to its oblique
141 convergence orientation and seismically inactive feature (Satake and Atwater, 2007).
142 Globally, the eventual ruptures of some unexpected fault locations keep surprising
143 scientists (Bilek and Lay, 2018). We've seen partial ruptures of fully locked megathrusts
144 (Konca et al., 2008; Qiu et al., 2016; Ruiz et al., 2014; Schurr et al., 2014), and piecemeal
145 breaks in the center of perceived seismic gaps (e.g. Salman et al., 2017). Even with
146 improved observations, it remains difficult to constrain the magnitude of potential
147 earthquake in the first order, and even more difficult to define the rupture pattern (e.g., Lay,
148 2018). A recent example comes from Japan where Loveless & Meade (2010) used a number
149 of inland GPS stations to estimate the coupling state of the Japan megathrust before the
150 2011 Tohoku-Oki earthquake. They indicated the spatial extent of a possible future rupture.
151 Notably, the rupture models constrained by multiple geodetic data sets after the 2011
152 earthquake (Koketsu et al., 2011; Loveless and Meade, 2011, Wei et al., 2012) are
153 significantly different to the coupling map of Loveless and Meade (2010). The discrepancy
154 between a coupling map and actual rupture estimates has also been observed at other
155 subduction zones (e.g. Ruiz et al., 2014; Schurr et al., 2014) and for the collision zone
156 between the Indian and Eurasian plates (Avouac et al., 2015; Qiu et al., 2016; Stevens and
157 Avouac, 2015). Clearly, our current knowledge of the seismogenic characteristics of giant
158 earthquakes remains deficient.

159



160 Great efforts have been made to investigate the physical parameters that characterize
161 subduction zones with regard to the geometry, geology and dynamics (Schellart and
162 Rawlinson, 2013). Systematic analysis of collections of great earthquakes globally indeed
163 suggests that some of the physical parameters do play key roles in controlling the rupture
164 characteristics (Bilek and Lay, 2018; Bletery et al., 2016; Schellart and Rawlinson, 2013).
165 Taking into account the geometrical effects, previous studies have divided the entire Manila
166 subduction zone into three segments (i.e. Zhu et al. 2013; Li et al. 2016; Gao et al. 2018).
167 Here we follow the segments proposed by Li et al. (2016), and we provide new constraints
168 on earthquake and tsunami potentials by combining geological information and the
169 geodetic constrained coupling map to adjust these segments accordingly. The modulated
170 three segments are 14°N-16°N, 16°N-19°N, 19°N-22°N, respectively. Their significances are
171 detailed in subsequent sections.

172 **2.1 Rupture segment 1 (zone 1, 14°N-16°N)**

173 The Manila trench primarily starts from ca.13°N west of Mindoro and ends at ca.22°N
174 southwest of Taiwan, and beyond these bounds the Manila trench gradually transform into
175 collision and accretionary belt in the north and south (Figure 1). At the southernmost area
176 of the Manila trench, the strike direction of the trench bends to southeast offshore the
177 Mindoro Island (ca.13°N) before it further collides with Panay (ca.11°N). Within this region
178 (ca.13°N to 11°N) the relocated seismicity suggest the subducting slab dips almost
179 vertically, with an absence of the deep seismicity (Bautista et al., 2001). Based on these
180 features, Bautista et al. (2001) suggest the subducting slab may have been heated up and
181 assimilated into the mantle. We, therefore, interpret that the great megathrust earthquake
182 is less likely south of 13°N. Li et al. (2016) placed the southern boundary of the first
183 segment at ca.12.5°N. While Bautista et al. (2001) proposed a slab tear at ca.14°N which is
184 the result of the collision of a micro-continental plate with Mindoro and Panay islands and
185 as evidenced by the narrow seismicity gap north of 14°N that trends northeastward (Figure
186 2). Based on these geological characteristics and geodetic measurements, together with the
187 fact that the spatial coverage of GPS measurements in this region only allows us to estimate
188 the coupling status starting at 14°N to the north (Hsu et al. 2016), we move the southern
189 boundary of the first segment from ca.12.5°N proposed by Li et al. (2016) to 14°N, but we



190 do not rule out the possibility of rupture cases that propagate across 14°N to 13°N or even
191 beyond.

192

193 Moving to the north, between 16°N to ca.17.5°N, a bathymetric high called Scarborough
194 seamount chain is subducting beneath the Philippine plate. The Scarborough seamount can
195 be traced between ca.12°N to 18°N from the subducting Sunda plate and between ca.16°N
196 to 19°N (Figure 1) after subducting beneath the Philippine plate from the regional
197 tomography model (Wu et al., 2016). This seamount chain has been interpreted as part of
198 an extinct Middle Ocean Ridge (MOR) that is either presently being accreted or subducted
199 under the trench at 16°N (Ludwig, 1970; Pautot and Rangin, 1989). A slab tear was
200 proposed at 16°N based on seismic-related strain energy release of intermediate-depth and
201 shape changes in the dip angle of the slab (Bautista et al., 2001). Although great
202 earthquakes can rupture across the seamounts or morphological bounds occasionally (e.g.
203 Bell et al., 2014; Duan, 2012; Kumagai et al., 2012), global observations suggest that in
204 many cases seamounts or barriers impede (Singh et al., 2011; Wang and Bilek, 2011) or
205 confine rupture propagations (Qiu et al., 2016). Further, we note that slab tears at 14°N and
206 16°N bound the southern and north tip of the highly coupled west Luzon trough (Hsu et al.,
207 2012, 2016) coincidentally, and these tears may act as morphological barriers to limit the
208 rupture propagation similar to that noted from the 2015 M_w 7.8 Nepal event (Qiu et al.,
209 2016). We, therefore, define the region between 14°N to 16°N as segment 1 (zone 1)
210 (Figure 3a and d).

211

212 **2.2 Rupture segment 2 (zone 2, 16°N-19°N)**

213 As noted in section 2.1, the Scarborough seamount chain is located between ca.16°N to
214 17.5°N where the subducting Sunda plate meets with the Philippine plate (Figure 1). A
215 regional tomography model also suggests that the subducted seamount chain can be traced
216 between ca.16°N to 19°N (Wu et al., 2016). In this subducted seamount region, the absence
217 of seismicity and seismic-related strain energy release at intermediate depths suggest the
218 possible trajectory of the MOR that is interpreted to be still hot and deforming plastically
219 (Bautista et al., 2001). Globally studies of subducting seamount systems suggest that large
220 fracture zones are formed surrounding the seamount, and the highly fractured region can



221 act as barriers to hinder the rupture propagation (e.g., Wang & Bilek 2011). Because the
222 stress concentration in and around the fracture zones is high and may easily reach failure
223 criteria, the seamount can trigger (e.g., Kumagai et al. 2012; Koyama et al. 2013) the failure
224 of highly stressed asperities in the neighborhood, nucleating as a great earthquake (e.g.,
225 Kumagai et al. 2012; Koyama et al. 2013). Previous studies also suggest that seamounts
226 cause persistent fault creep (e.g., Singh et al. 2011) or rupture as small earthquakes due to
227 localized areas of high fracture and associated regional stress anomalies (e.g., Wang & Bilek
228 2011). Thus, fault creep and the rupture of single or multiple asperities are all possible in
229 this region.

230

231 The Geodetic coupling map constrained by long-term GPS velocity measurements indicates
232 that the seamount chain region (i.e. ca.16°N to 19°N) is less coupled (Figure 3, coupling
233 models A and B), partially due to the fault creep caused by the seamounts or poor
234 constraints by paucity of the offshore observations (Hsu et al., 2012, 2016). The weak
235 coupling extends further north to 19°N, in the area of the southern tip of the North Luzon
236 Trough and west of the northern tip of Luzon Island. This area is likely creeping or weakly
237 coupled (Figure 3, coupling mode A and B). Additionally a trench-parallel gravity anomaly
238 (TPGA) has been interpreted with great subduction earthquakes occurring predominately
239 in areas characterized by strongly negative TPGA, while regions with strongly positive
240 TPGA are relatively aseismic (Song and Simons, 2003). We note that positive TPGA covers
241 from ca.16°N to 19°N (Hsu et al., 2012), coinciding with the geodetically determined
242 weakly coupled and creep regions. Considering all these factors mentioned above, we
243 redefine segment 2 (zone 2) as the region between 16°N to 19°N as (Figure 3b and e)
244 slightly extends further north when compared with the same segment of Li et al. (2016).

245

246 **2.3 Rupture segment 3 (zone 3, 19°N-22°N)**

247 The area of the megathrust bounded between the southern tip of Taiwan and northern
248 Luzon (between 19°N to 22°N) (Figure 1) is poorly understood, as the current available
249 geodetic measurements are sparse and primarily deployed in the volcanic islands to the
250 east which are far away from the Manila trench (Hsu et al., 2012, 2016). In this region, the
251 Manila trench bends sharply at 20°N (Figure 1). Geologically the bending has been



252 interpreted as the result of the subduction of a high-relief bathymetrical plateau that is
253 sufficient buoyant to impede subduction (Bautista et al., 2001; Suppe, 1988) or may due to
254 thick sediments (Lin et al., 2009). Additionally, here regional block faulting stretches the
255 continental crust, resulting in numerous micro-continental fragments. Further, the 1980s
256 geophysical studies (Taylor and Hayes, 2013) have recovered a magnetic quiet zone
257 characterized to the continental-to-oceanic boundary (Bautista et al., 2001), and this zone
258 was further interpreted with a transition zone between a continental and oceanic
259 lithosphere (Taylor and Hayes, 2013). If these numerous fragments are indeed subducting
260 beneath the Philippine sea plate, then they would have be buoyant enough to resist the
261 subducting process at 20°N with fast subducting of the neighboring portions of the trench
262 that may extending south to 19°N. Such a situation would result a complex stress field in
263 the upper plates that were mirrored by diverse and complicated focal mechanism solutions
264 (Bautista et al., 2001).

265

266 As more marine geophysical data becomes available, there is an increased understanding of
267 the geological structure and potential seismogenic faults (Lin et al., 2009). Detailed
268 analysis of seismic reflection data (i.e. Line 973 in Lin et al. 2009) reveals prominent
269 seismogenic structures in the region, which include frontal décollement beneath the lower-
270 slip domain and out-of-sequence thrusts (OOST) in lower- and upper-slope domains (Lin et
271 al., 2009; Zhu et al., 2013). Evidence from the thermal regime of these structures suggests
272 that the megathrust and part of the frontal décollement are seismogenic (Lin et al., 2009).
273 These seismogenic structures are found to be analogous to that observed in the Nankai
274 prism of the Nankai Trough, Japan, posing potentials for generating great earthquakes and
275 tsunamis as they did in Nankai (Lin et al., 2009; Yokota et al., 2016).

276

277 Fan et al. (2016) revealed a low-velocity zone that spans from shallow to deep depths of
278 20-200km beneath the prism, suggesting that the collision develops northward and the
279 subducting process may stop at 22°N. Coincidentally, at the similar latitude (21.5°N), Lin et
280 al. (2009) interpret that south of 21.5°N, the subducting is active while north of this
281 latitude the plate convergence is accommodated by intense compressional deformation of
282 the crust due to the buoyance of the Eurasian plate that resists subduction. Consequently,
283 in light of the geological evidence noted above, we slightly shorten the northern boundary



284 of the segment 3 from Li et al. (2016), and we define the region to be between 19°N to
285 21.7°N as the segment 3 (zone 3) (Figure 3c and f).

286

287 **3. Proposed slip deficit models**

288 Using geodetic surface measurements, velocity value can be derived and used to constrain
289 the elastic strain accumulation rate between the subduction plate interfaces, the so-called
290 interseismic coupling model (Chlieh et al., 2008; Hsu et al., 2012, 2016; Loveless and
291 Meade, 2010; Megawati et al., 2009). This model reveals strain accumulation within seismic
292 cycles that can potentially be released during great earthquakes, although the final rupture
293 extent is commonly not exactly the same as forecasted by the coupling maps (Konca et al.,
294 2008; Ruiz et al., 2014). However to move towards an associated tsunami hazard
295 assessment from such potential ruptures, the coupling map though not the perfect is often
296 the necessary choice (e.g., Power et al. 2012; Megawati et al. 2009).

297

298 Using decades-long GPS velocity measurements, Hsu et al. (2016) proposed two coupling
299 models (A and B) that best explain the plate movements and coupling state on the Manila
300 megathrust and other faults on the Luzon island. With this coupling or slip deficit rate
301 estimates and the possible seismic return time period, we can forecast the likely slip
302 distributions that may fail in future earthquakes. To gain a comprehensive understanding
303 of the seismic return time period, large amount of historical seismic data and geological
304 evidence are required. The modern seismic records for the Manila trench only trace back to
305 ~1900 and provide constraints on the natural frequency of earthquakes with its
306 corresponding magnitude assuming the Gutenberg-Richter (G-R) earthquake relations, and
307 thus often implemented for tsunami hazard assessment (Li et al., 2016; Power et al., 2012).
308 Historical records since the 1560s suggest that there is no recorded earthquake with $M_w >$
309 7.6 in the Manila subduction zone, implying that the determined return time period for
310 great earthquake from G-R relation will likely poorly constrained (Hsu et al., 2016).
311 However geological evidence from purported tsunami deposits may provide evidence of
312 tsunamis at four locations in SCS (i.e. Figure 1, Ramos et al. 2017; Sun et al. 2013; Yu et al.
313 2009; Yang et al. 2018). Some studies suggest that a giant tsunami event might have
314 occurred ca.1000-1064 AD (Ramos et al., 2017; Tang et al., 2018). With an assumption of a-



315 1000-year return period, the magnitude can reach M_w 9+ from geodetic analysis (Hsu et al.,
316 2016). We, thus, use the only available information that the seismic return period is likely
317 to be ca.1000 year and a giant event had ruptured the Manila trench in the last seismic
318 cycle.

319

320 Based on coupling models A and B of Hsu et al. (2016) in which the spatial distribution of
321 slip rate and coupling rate are available, we use a return period 1000 years to calculate the
322 slip deficit of great earthquakes. For the predefined zones 1 to zone 3 (see sections 2.1-2.3),
323 different approaches are used. For zones 1 and zone 2 where the coupling ratios and slip
324 rate are relatively better constrained than zone 3, we calculate the slip deficit by
325 multiplying the slip deficit rate at each triangle node (Figure 3a, b d and e) with 1000 years.
326 The slip deficit models in zone 1 for models A and B (Figure 3a and d) are similar with the
327 maximum slip >50 meters occurred at ca.20-30km seismogenic depth due to the high
328 coupling ratio. For zone 2, the slip model based on A has a compact area and less slip
329 amount as compared with slip model based on B (Figure 3b and e). This is because the
330 extra north Luzon trough fault was introduced in model B, resulting in larger spatial extent
331 and higher coupling while equally explaining the GPS velocity measurements (Hsu et al.,
332 2016).

333

334 Due to paucity of observations in zone 3, no coupling ratios were resolved. Geologically this
335 zone is much more complicated than zones 1 and 2 (Lin et al., 2009). Multiple OOSTs are
336 revealed from seismic reflection profiles (Lin et al., 2009; Zhu et al., 2013). Failure of these
337 OOSTs (or called megasplay) faults with high dip angle contributes to generating
338 devastating waves as evidenced from historic tsunami events in other subduction zones
339 (Moore et al., 2007; Park et al., 2002). It is, therefore, crucial but difficult to precisely
340 quantify individual role of the OOSTs and megathrust in tsunami generation.

341

342 We propose two end-member scenarios, considering different rupture modes in zone 3
343 with two steps. We first calculate the slip deficit from the slip deficient rate of models A and
344 B between 19°N to 20°N. We then consider two end-member scenarios in the region from
345 20°N to 21.7°N. The first-member is the seismogenic events with rupture depths
346 determined from a collection of GCMT solutions of the world megathrust earthquakes



347 (Figure 4). We assume the fault slip pattern follows a Gaussian distribution centered at 25
348 km of the mean depth from the global great earthquakes. We cutoff slip deeper than 50 km
349 as the rock properties at this depth and beyond behave semi-brittle and ductile flow
350 (Hippchen and Hyndman, 2008; Hyndman and Wang, 1993; Wang, 2007). By doing so it
351 could capture the first-order of potential slip extent (Figure 3c and f), similar as the
352 estimated depth-range of slip observed from global megathrust great earthquakes (e.g.,
353 Chlieh et al. 2007; Pollitz et al. 2011; Ruiz et al. 2014; Salman et al. 2017; Wei et al. 2012).
354 For the second mode, we consider tsunamigenic events similar to 2011 M_w 9.0 Japan
355 earthquake in which the earthquake can rupture all the way to the trench. We estimate the
356 plate convergence rate in the fore-arc in zone 3 is 67 mm/year (Hsu et al., 2009) with a
357 24.5 mm/year shortening under the 91.5 mm/year plate convergence rate with respect to
358 Sunda plate (Hsu et al., 2016; Sella et al., 2002). We assume 67 mm/year convergence was
359 fully accommodated by the megathrust and implement it as the amplitude of the Gaussian
360 distribution, allowing the maximum slip occurring at the trench (Figure 5a and b). For each
361 rupture mode, we have two slip models corresponding to coupling model A and B, and
362 assume half of plate convergence rate are accommodated by the megathrust (Figures 5a
363 and b, with 80% coupling ratio shown in Figure 6c and d). For the second-member model,
364 we implement rupture on both the megasplay fault and the megathrust assuming each of
365 them accommodating half of the fore-arc plate convergence and a uniform slip on the splay
366 fault as a simple case (Figure 5c and d). We implement this splay fault only with
367 seismogenic rupture events as we think this case is easier due to splay fault's bottom cut to
368 the megathrust at seismogenic depth (Lin et al., 2009). We consider a 50% coupling ratio
369 on both the megathrust and splay fault (Figure 5c and d, with 80% coupling shown in
370 Figure 6a and b). Details about these proposed rupture scenarios are given in the summary
371 Table S1 in the supplementary file.

372

373 The geometry of the OOST is derived from Lin et al. (2009) and covers the area from 20°N
374 to ca.22.2°N, as we ignored the bending portions of the OOST in the north and south
375 although they still can rupture with a low probability. The fault is ca.260 km long, ca.16 km
376 wide, and it strikes 345° to the north and dips 50° to the east (Figures 1, 5 and 6).



377 4. Tsunami impacts in SCS

378 4.1 Tsunami simulation set up

379 We use **Cornel Multi-grid Coupled Tsunami** model (COMCOT) to simulate the
380 hydrodynamic process of the tsunami waves (e.g., Wang et al. 2008; Philip 1994; Li et al.
381 2018; Li et al. 2016) produced by those proposed earthquake ruptures (The initial surface
382 elevations generated by all the proposed rupture models can be found in Supplementary
383 data). To account for the nonlinear effect in nearshore region, the simulation solves non-
384 linear shallow water equations in spherical coordinates for the entire SCS region with a
385 bottom Manning friction coefficient of 0.013 (Li et al., 2018). We used the 1 arc-minute grid
386 of General Bathymetric Chart of the Oceans (GEBCO) data for the modeling. We considered
387 one grid layer for each case to model wave propagations in the SCS because we don't focus
388 in near- and on-shore processes where high-resolution topographical data and good
389 understanding of the bottom friction effect are required. Synthetic gauges along 20-m
390 isobaths are specified to record the tsunami waveforms. For the initial tsunami waves, we
391 assume the rupture occurs instantaneously and the vertical seafloor deformation produced
392 by the ruptures is used to simulate the tsunami wave propagations (e.g., Li et al. 2016; Li et
393 al. 2018; Liu et al. 2009).

394 4.2 Maximum tsunami wave height

395 For all the simulated scenarios, the resulting wave height in the near-source regions mainly
396 depends on the rupture location and earthquake magnitude. While in the relatively far-
397 field, the tsunami wave directivity effects and bathymetry effects also play important roles
398 (Figures 7 and 8). We describe the tsunami impact of each pair of source models from
399 south (zone 1) to north (zone 3). Slip models in zone 1 generate the largest tsunami waves
400 (>10m) in western Luzon (Figure 7a-b). Central Vietnam experiences a similar tsunami
401 height (4-8 m) with the intermediate far-field area, western Palawan. Southeastern China
402 and southern Taiwan could be attacked with up to 5 m tsunami waves (Figure 7a-b).
403 Moving to zone 2, the slip models show the significant difference in terms of both
404 magnitude and slip distribution between models A and B (Figure 3b and Figure 3e).
405 Consequently, the tsunami impact caused by model B is much larger than the one caused by
406 model A in both near-source (e.g., western Luzon and southern Taiwan) and far-field



407 regions (e.g. southeastern China and central Vietnam). Compared with the most affected
408 region by slip models in zone 1, the worst-hit region also moves northward with the
409 rupture location. Similarly, when the earthquakes rupture the megathrust in zone 3, the
410 hardest-hit regions move further to the northern part of the SCS and concentrate in
411 northern Luzon, southern Taiwan and southeastern China (Figure 7e-f). Further, Figure 8
412 shows the diverse tsunami impacts generated by rupture scenarios in zone 3. Not
413 surprisingly, the results suggest rupture models with higher coupling cases (Figure 8a-b)
414 result larger tsunami wave heights in regions located in northeast SCS despite of the
415 tsunami generation efficacy of shallow slip earthquakes (Figure 8c-d). One interesting
416 phenomenon worthy of mention is the high tsunami hazard of the southeastern China
417 regardless of the rupture locations. This is likely explained by the combined effect of
418 tsunami wave directivity and bathymetry (Figures 7 and Figure 8). Tsunami waves refract
419 significantly in the southern Chinese coast due to the shape and gradient of the continental
420 slope, leaving southeastern China (including coastlines of Guangdong, Hong Kong, and
421 Macau) in the direct tsunami path.

422

423 To summarize, the near-source regions including western Luzon, northern Luzon and
424 southern Taiwan face the greatest tsunami hazard. The second most threatened areas are
425 southeastern China, central Vietnam and western Palawan. Archipelagos inside the SCS
426 including Dongsha, Zhongsha and Xisha also suffer severe tsunami attacks (up to 6-8 m
427 tsunami wave height) when large earthquakes occur in zones 2 and 3. Coastal regions of
428 northern Borneo, eastern Malaysia, eastern Thailand, and southern Cambodia are
429 significantly less affected.

430

431 **4.3 Tsunami travel time**

432 Potential tsunami arrival time is key information in tsunami evacuation planning. Similar to
433 the other subduction zones, the near-source areas including the coast of Luzon and
434 southern Taiwan suffer the highest tsunami waves with least evacuation time (Figures 7
435 and 8). We plot the time series of tsunami wave generated by all the source models in
436 selected synthetic gauges near 9 major coastal cities in Figure 9. Depending on the rupture
437 locations, the tsunami arrival time is in minutes or less than half an hour for near-source



438 cities, like Vigan, Kenting and Kaohsiung (Figure 9), posing great challenges to the early
439 warning system and subsequent evacuation process. In other areas tsunami wave travel
440 time is relatively longer for example Vietnam and southeastern China. The arrival time is
441 commonly between 2-3 hours after the earthquake for central Vietnam and 3-4 hours for
442 southern China. For the Archipelagos inside the SCS, the tsunami waves arrive much earlier
443 than they do on the mainland in Vietnam and China, typically ~1 hour earlier. The earlier
444 arrival time in archipelagos make them ideal locations for installing tsunami monitoring
445 instruments (e.g. tide gauges or GPS (see Peng et al., 2019)), as. Such measurements may
446 provide timely constraints on wave height for the evacuations in far-field areas further
447 afield. Detailed inundation maps of the main coastal cities in this region are highly
448 recommended for designing evacuation route.

449

450 5. Discussion

451 How and where earthquake rupture will occur on a plate boundary is challenging to
452 forecast (Bilek and Lay, 2018; Satake and Atwater, 2007). A comprehensive understanding
453 of a single megathrust behavior may be impractical since the seismic cycle is typically in
454 the order of hundreds and thousands of years, much longer than instrumental records.
455 Whereas understanding megathrust behaviors over different subduction zones at different
456 time stages of their cycle offers insights into rupture style and characteristics. Previous
457 studies have intensively investigated giant subduction zone earthquakes, gaining useful
458 insights into physical parameters that are related to developing giant ruptures. Such
459 physical parameters include the subducting plate age, rate and buoyance of the slab
460 (Kanamori, 2006; Nishikawa and Ide, 2014; Ruff and Kanamori, 1980, 1983); the forearc
461 structures (Song and Simons, 2003; Wells et al., n.d.), upper plate characteristics including
462 plate motion (Schellart and Rawlinson, 2013), trench characteristics of the long-term
463 migration (Schellart and Rawlinson, 2013) and sediments thickness (Heuret et al., 2012),
464 and the width of seismogenic zones (Hayes et al., 2012; Schellart and Rawlinson, 2013).
465 Recently a summary study based on global subduction zone observations concludes that
466 mega-seismic events preferentially rupture flat gentle dipping interface (Bletery et al.,
467 2016). In the Manila trench, the dipping is gentle and progressively increases from north to
468 south (Bautista et al., 2001). In zone 3, the presence of subducting plateau of the



469 continental fragments results in a gently dipping, near flat interface that potentially favors
470 the development of giant earthquakes (Figures 1 and 2). The dipping degree is in a similar
471 range with those found in other subduction zones, e.g., Japan-Kuril-Kamchatka, Alaska-
472 Aleutians, Sumatra-Java, South American, and Cascadia, which are known to produce $M_w >$
473 9.0 earthquakes (Bletery et al., 2016).

474

475 Morphological barriers have been found to have a predominant role in controlling rupture
476 propagation and style. The barriers can confine and arrest rupture propagation (Qiu et al.,
477 2016), and act be a persistent fence to stop rupture (Meltzner et al., 2012; Morgan et al.,
478 2017). Faults bends can also hinder rupture overstep at bending points (Wesnousky, 1988,
479 2006). In the case of the Manila subduction zone, the presence of Scarborough Seamount
480 chain in zone 2 and slab tear in zone 1 indicates that a giant rupture propagation through
481 zones 3 to 1 is less likely, although we do acknowledge that the rupture-across-zone
482 earthquake is possible with very low probability. Dynamic simulations do show possible
483 scenarios that involve multiple portions of the Manila trench rupturing as a single giant
484 earthquake (Yu et al., 2018). However, the details of the slab tear in zone 1 and the
485 seamount chain in zone 2 were smoothed out in the simulation, due to the challenges of the
486 numerical calculation (Yu et al., 2018).

487

488 Regarding the potential source of the geological records, the tsunami simulations suggest
489 the difficulty of creating a scenario which could affect all the four tsunami deposit locations
490 with sufficiently high tsunami waves, especially for the record located in Yongshu island (Yu
491 et al., 2009). Assuming all the four records are indeed tsunami deposits, the spatial
492 distribution demands the whole trench to rupture at once and the southern segment needs
493 to extend further to 13° in order to generate tsunami waves propagation southwest
494 direction towards Yongshu. Another alternative explanation could be that the deposits in
495 Yongshu island were generated by large storm event instead of tsunami event.

496

497 In summary, our definition of the rupture zones 1, 2 and 3 are derived by taking into
498 account the bathymetry features of the subduction Eurasian plate, earthquake focal
499 mechanisms distributions, structure controlled TPGA and more than 20-year-long GPS
500 measurements. The refined coupling models (Hsu et al., 2016) offer more detailed images



501 that reflect the likely motions on the plate interface. Combination of the coupling models
502 and morphological bounds constrained zone definitions provide more realistic rupture
503 scenarios than previously assumed planar fault rupture cases with spatial uniform slip.
504 Heterogeneous slip models, as we observe from finite rupture models of earthquakes, are
505 more realistic and could better explain the observations. Further detailed tsunami hazard
506 assessment in SCS demonstrates that uniform slip models underpredict tsunami hazards as
507 compared to a heterogeneous slip model (Li et al., 2016). Therefore, our refined
508 earthquake rupture cases in zones 1 and 2 provide a new standard of scenarios for tsunami
509 hazard assessment in SCS. For zone 3, the scarcity of measurements and the presence of
510 complicated geological structures result in a poor understanding of the seismogenic
511 characteristics, although the tsunami-genic potential remains high (Lin et al., 2009). The
512 possible ruptures provided in this study can be a first-order approximation of the
513 earthquake scenarios in the region. Subsequent measurements collected in coming years
514 can help us to refine our understanding in this region.

515
516

517 **6. Conclusion**

518 We have proposed updated earthquake rupture scenarios along the Manila trench based on
519 new geological, earthquake focal mechanisms information and geodetic observations.
520 These rupture models provide new constraints for tsunami assessment in SCS, and
521 subsequent detailed examination on inundation process for mega-cities along the
522 coastlines of SCS.

523

524 Tsunami simulations based on these rupture scenarios indicate that the coastlines of the
525 SCS region are under a risk of devastating tsunami waves, specifically for western Luzon of
526 Philippine, southern Taiwan, the southeastern China, central Vietnam, and Palawan Island.
527 Besides the near-source region, the southeastern China will also be attacked severely due
528 to the bathymetry focusing effect no matter which portion of the Manila thrust breaks.
529 Southern Taiwan is affected by ruptures in zones 2 and 3, with west Luzon affected by all
530 earthquake scenarios. Central Vietnam and Palawan Island are mostly affected by ruptures
531 in zones 1 and 2. In all cases, the waves sweep these coastlines within ca.3 hours. Our



532 results highlight that it is necessary to conduct further detailed inundation investigations at
533 these severely affected coastal regions, for future preparation on hazard mitigation plans.
534 Our findings also provide useful information that could be used to find possible archived
535 geological recordings of historical tsunami deposits, and call for following paleo-
536 sedimentology studies in the SCS basin.

537 **Author contribution:** QQ, LL, YH and YW developed the method of calculating the fault
538 parameters. QQ performed the tsunami simulations. QQ and LL prepared the manuscript
539 with contributions from all co-authors.

540 **Acknowledgements**

541 This study is supported by Guangdong Province Introduced Innovative R&D Team of
542 Geological Processes and Natural Disasters around the South China Sea (2016ZT06N331),
543 National Natural Science Foundation of China (41774049, 41590861). This study is also
544 supported by a Joint project “Probabilistic tsunami hazard assessment in South China Sea
545 region” between National University of Singapore and Shang Hai Jiao Tong University. This
546 project is funded by Singapore National Research Fund and National Natural Science
547 Foundation of China. ADS thanks the support of Scor RE through a donation. We thank Ms
548 Constance T. Chua for the English proofreading. The GEBCO data used in this study were
549 downloaded from www.gebco.net in October 2014. All data needed to evaluate the
550 conclusions in the paper are present in the paper and/or the Supplementary Materials. We
551 provide files of initial surface elevations generated by the proposed fault models in the
552 Supplementary Materials. Readers can download these files for tsunami simulation.
553 Additional data related to this paper can be requested from the authors through email.

554

555 **References**

556 Avouac, J.-P., Meng, L., Wei, S., Wang, T. and Ampuero, J.-P.: Lower edge of locked Main
557 Himalayan Thrust unzipped by the 2015 Gorkha earthquake, *Nat. Geosci.*, 8, 708 [online]
558 Available from: <https://doi.org/10.1038/ngeo2518>, 2015.
559 Banerjee, P., Pollitz, F., Nagarajan, B. and Bürgmann, R.: Coseismic Slip Distributions of the
560 26 December 2004 Sumatra-Andaman and 28 March 2005 Nias Earthquakes from gps
561 Static Offsets, *Bull. Seismol. Soc. Am.*, 97(1A), S86–S102, doi:10.1785/0120050609, 2007.
562 Bautista, B. C., Bautista, M. L. P., Oike, K., Wu, F. T. and Punongbayan, R. S.: A new insight on
563 the geometry of subducting slabs in Northern Luzon, Philippines, *Tectonophysics*,



- 564 doi:10.1016/S0040-1951(01)00120-2, 2001.
- 565 Bautista, M. L. P., of Volcanology, P. I. and Seismology: Philippine Tsunamis and Seiches,
566 1589 to 2012, Department of Science and Technology, Philippine Institute of Volcanology
567 and Seismology. [online] Available from:
568 <https://books.google.com.sg/books?id=OHibnQAACAAJ>, 2012.
- 569 Bell, R., Holden, C., Power, W., Wang, X. and Downes, G.: Hikurangi margin tsunami
570 earthquake generated by slow seismic rupture over a subducted seamount, Earth Planet.
571 Sci. Lett., 397, 1–9, doi:<https://doi.org/10.1016/j.epsl.2014.04.005>, 2014.
- 572 Bilek, S. L. and Lay, T.: Subduction zone megathrust earthquakes, Geosphere, 14(4), 1468–
573 1500, doi:10.1130/GES01608.1, 2018.
- 574 Bletery, Q., Thomas, A. M., Rempel, A. W., Karlstrom, L., Sladen, A. and De Barros, L.: Mega-
575 earthquakes rupture flat megathrusts, Science 80, doi:10.1126/science.aag0482, 2016.
- 576 Chlieh, M., Avouac, J. P., Hjorleifsdottir, V., Song, T. R. A., Ji, C., Sieh, K., Sladen, A., Hebert, H.,
577 Prawirodirdjo, L., Bock, Y. and Galetzka, J.: Coseismic slip and afterslip of the great Mw 9.15
578 Sumatra-Andaman earthquake of 2004, Bull. Seismol. Soc. Am., 97(1A), S152–S173,
579 doi:10.1785/0120050631, 2007.
- 580 Chlieh, M., Avouac, J. P., Sieh, K., Natawidjaja, D. H. and Galetzka, J.: Heterogeneous coupling
581 of the Sumatran megathrust constrained by geodetic and paleogeodetic measurements, J.
582 Geophys. Res., 113(B5), 1–31, doi:10.1029/2007JB004981, 2008.
- 583 Cifuentes, I. L.: The 1960 Chilean earthquakes, J. Geophys. Res. Solid Earth, 94(B1), 665–
584 680, doi:10.1029/JB094iB01p00665, 1989.
- 585 Duan, B.: Dynamic rupture of the 2011 Mw 9.0 Tohoku-Oki earthquake: Roles of a possible
586 subducting seamount, J. Geophys. Res. Solid Earth, 117(5), doi:10.1029/2011JB009124,
587 2012.
- 588 Fan, J., Zhao, D. and Dong, D.: Subduction of a buoyant plateau at the Manila Trench:
589 Tomographic evidence and geodynamic implications, Geochemistry, Geophys. Geosystems,
590 doi:10.1002/2015GC006201, 2016.
- 591 Gao, J., Wu, S., Yao, Y., Chen, C., Song, T., Wang, J., Sun, J., Zhang, H., Ma, B. and Yangbing, X.:
592 Tectonic deformation and fine structure of the frontal accretionary wedge, northern Manila
593 subduction zone, Chinese J. Geophys. Chinese Ed., 61, 2845–2858,
594 doi:10.6038/cjg2018L0461, 2018.
- 595 Hayes, G. P., Wald, D. J. and Johnson, R. L.: Slab1.0: A three-dimensional model of global



- 596 subduction zone geometries, *J. Geophys. Res. Solid Earth*, 117(B1),
597 doi:10.1029/2011JB008524, 2012.
- 598 Heuret, A., Conrad, C. P., Funicello, F., Lallemand, S. and Sandri, L.: Relation between
599 subduction megathrust earthquakes, trench sediment thickness and upper plate strain,
600 *Geophys. Res. Lett.*, doi:10.1029/2011GL050712, 2012.
- 601 Hippchen, S. and Hyndman, R. D.: Thermal and structural models of the Sumatra
602 subduction zone: Implications for the megathrust seismogenic zone, *J. Geophys. Res. Solid*
603 *Earth*, 113(B12), doi:10.1029/2008JB005698, 2008.
- 604 Hong Nguyen, P., Cong Bui, Q., Ha Vu, P. and The Pham, T.: Scenario-based tsunami hazard
605 assessment for the coast of Vietnam from the Manila Trench source, *Phys. Earth Planet.*
606 *Inter.*, doi:10.1016/j.pepi.2014.07.003, 2014.
- 607 Hsu, Y.-J., Yu, S.-B., Simons, M., Kuo, L.-C. and Chen, H.-Y.: Interseismic crustal deformation
608 in the Taiwan plate boundary zone revealed by GPS observations, seismicity, and
609 earthquake focal mechanisms, *Tectonophysics*, 479(1), 4–18,
610 doi:<https://doi.org/10.1016/j.tecto.2008.11.016>, 2009.
- 611 Hsu, Y.-J., Yu, S.-B., Song, T.-R. A. and Bacolcol, T.: Plate coupling along the Manila
612 subduction zone between Taiwan and northern Luzon, *J. Asian Earth Sci.*, 51, 98–108,
613 doi:<https://doi.org/10.1016/j.jseaes.2012.01.005>, 2012.
- 614 Hsu, Y.-J., Yu, S.-B., Loveless, J. P., Bacolcol, T., Solidum, R., Luis Jr, A., Pelicano, A. and
615 Woessner, J.: Interseismic deformation and moment deficit along the Manila subduction
616 zone and the Philippine Fault system, *J. Geophys. Res. Solid Earth*, 121(10), 7639–7665,
617 doi:10.1002/2016JB013082, 2016.
- 618 Hyndman, R. D. and Wang, K.: Thermal constraints on the zone of major thrust earthquake
619 failure: the Cascadia Subduction Zone, *J. Geophys. Res.*, doi:10.1029/92JB02279, 1993.
- 620 Johnson, J. M. and Satake, K.: Asperity Distribution of the 1952 Great Kamchatka
621 Earthquake and its Relation to Future Earthquake Potential in Kamchatka, in *Seismogenic*
622 *and Tsunamigenic Processes in Shallow Subduction Zones*, edited by J. Sauber and R.
623 Dmowska, pp. 541–553, Birkhäuser Basel, Basel., 1999.
- 624 Kanamori, H.: Re-examination of the earth's free oscillations excited by the Kamchatka
625 earthquake of November 4, 1952, *Phys. Earth Planet. Inter.*, 11(3), 216–226, 1976.
- 626 Kanamori, H.: Lessons from the 2004 Sumatra-Andaman earthquake, *Philos. Trans. R. Soc.*
627 *A Math. Phys. Eng. Sci.*, 364(1845), 1927–1945, doi:10.1098/rsta.2006.1806, 2006.



- 628 Koketsu, K., Yokota, Y., Nishimura, N., Yagi, Y., Miyazaki, S., Satake, K., Fujii, Y., Miyake, H.,
629 Sakai, S., Yamanaka, Y. and Okada, T.: A unified source model for the 2011 Tohoku
630 earthquake, *Earth Planet. Sci. Lett.*, 310(3–4), 480–487, doi:10.1016/j.epsl.2011.09.009,
631 2011.
- 632 Konca, A. O., Avouac, J.-P., Sladen, A., Meltzner, A. J., Sieh, K., Fang, P., Li, Z., Galetzka, J.,
633 Genrich, J., Chlieh, M., Natawidjaja, D. H., Bock, Y., Fielding, E. J., Ji, C. and Helmberger, D. V.:
634 Partial rupture of a locked patch of the Sumatra megathrust during the 2007 earthquake
635 sequence., *Nature*, 456(7222), 631–5, doi:10.1038/nature07572, 2008.
- 636 Koyama, J., Yoshizawa, K., Yomogida, K. and Tsuzuki, M.: Variability of megathrust
637 earthquakes in the world revealed by the 2011 Tohoku-oki Earthquake, *Earth, Planets Sp.*,
638 64(12), 13, doi:10.5047/eps.2012.04.011, 2013.
- 639 Kumagai, H., Pulido, N., Fukuyama, E. and Aoi, S.: Strong localized asperity of the 2011
640 Tohoku-Oki earthquake, Japan, *Earth, Planets Sp.*, 64(7), 649–654,
641 doi:10.5047/eps.2012.01.004, 2012.
- 642 Lau, A. Y. A., Switzer, A. D., DomineyHowes, D., Aitchison, J. C. and Zong, Y.: Written records
643 of historical tsunamis in the northeastern South China Sea-challenges associated with
644 developing a new integrated database, *Nat. Hazards Earth Syst. Sci.*, 10, 1793--1806,
645 doi:10.5194/nhess-10-1793-2010, 2010.
- 646 Lay, T.: A review of the rupture characteristics of the 2011 Tohoku-oki Mw 9.1 earthquake,
647 *Tectonophysics*, 733, 4–36, doi:<https://doi.org/10.1016/j.tecto.2017.09.022>, 2018.
- 648 Li, L., Switzer, A. D., Chan, C. H., Wang, Y., Weiss, R. and Qiu, Q.: How heterogeneous
649 coseismic slip affects regional probabilistic tsunami hazard assessment: A case study in the
650 South China Sea, *J. Geophys. Res. Solid Earth*, doi:10.1002/2016JB013111, 2016.
- 651 Li, L., Switzer, A. D., Wang, Y., Chan, C.-H., Qiu, Q. and Weiss, R.: A modest 0.5-m rise in sea
652 level will double the tsunami hazard in Macau, *Sci. Adv.*, 4(8), doi:10.1126/sciadv.aat1180,
653 2018.
- 654 Lin, A. T., Yao, B., Hsu, S.-K., Liu, C.-S. and Huang, C.-Y.: Tectonic features of the incipient arc-
655 continent collision zone of Taiwan: Implications for seismicity, *Tectonophysics*, 479(1), 28–
656 42, doi:<https://doi.org/10.1016/j.tecto.2008.11.004>, 2009.
- 657 Liu, P. L. F., Wang, X. and Salisbury, A. J.: Tsunami hazard and early warning system in South
658 China Sea, *J. Asian Earth Sci.*, doi:10.1016/j.jseaes.2008.12.010, 2009.
- 659 Loveless, J. P. and Meade, B. J.: Geodetic imaging of plate motions, slip rates, and



- 660 partitioning of deformation in Japan, , 115(B2), B02410, doi:10.1029/2008JB006248, 2010.
- 661 Loveless, J. P. and Meade, B. J.: Spatial correlation of interseismic coupling and coseismic
662 rupture extent of the 2011 MW = 9.0 Tohoku-oki earthquake, *Geophys. Res. Lett.*, 38(17),
663 doi:10.1029/2011GL048561, 2011.
- 664 Ludwig, W. J.: The Manila Trench and West Luzon Trough—III. Seismic-refraction
665 measurements, *Deep Sea Res. Oceanogr. Abstr.*, 17(3), 553–571,
666 doi:[https://doi.org/10.1016/0011-7471\(70\)90067-7](https://doi.org/10.1016/0011-7471(70)90067-7), 1970.
- 667 McCaffrey, R.: Global frequency of magnitude 9 earthquakes, *Geology*, 36(3), 263,
668 doi:10.1130/G24402A.1, 2008.
- 669 Megawati, K., Shaw, F., Sieh, K., Huang, Z., Wu, T. R., Lin, Y., Tan, S. K. and Pan, T. C.: Tsunami
670 hazard from the subduction megathrust of the South China Sea: Part I. Source
671 characterization and the resulting tsunami, *J. Asian Earth Sci.*,
672 doi:10.1016/j.jseaes.2008.11.012, 2009.
- 673 Meltzner, A. J., Sieh, K., Chiang, H.-W., Shen, C.-C., Suwargadi, B. W., Natawidjaja, D. H.,
674 Philibosian, B. and Briggs, R. W.: Persistent termini of 2004- and 2005-like ruptures of the
675 Sunda megathrust, , 117(B4), B04405, doi:10.1029/2011JB008888, 2012.
- 676 Moore, G. F., Bangs, N. L., Taira, A., Kuramoto, S., Pangborn, E. and Tobin, H. J.: Three-
677 Dimensional Splay Fault Geometry and Implications for Tsunami Generation, *Science* 80,
678 318(5853), 1128–1131, doi:10.1126/science.1147195, 2007.
- 679 Moreno, M. S., Bolte, J., Klotz, J. and Melnick, D.: Impact of megathrust geometry on
680 inversion of coseismic slip from geodetic data: Application to the 1960 Chile earthquake,
681 *Geophys. Res. Lett.*, 36(16), doi:10.1029/2009GL039276, 2009.
- 682 Morgan, P. M., Feng, L., Meltzner, A. J., Lindsey, E. O., Tsang, L. L. H. and Hill, E. M.: Sibling
683 earthquakes generated within a persistent rupture barrier on the Sunda megathrust under
684 Simeulue Island, *Geophys. Res. Lett.*, 44(5), 2159–2166, doi:10.1002/2016GL071901,
685 2017.
- 686 Nishikawa, T. and Ide, S.: Earthquake size distribution in subduction zones linked to slab
687 buoyancy, *Nat. Geosci.*, 7(12), 904–908, doi:10.1038/ngeo2279, 2014.
- 688 Okal, E. A., Synolakis, C. E. and Kalligeris, N.: Tsunami simulations for regional sources in
689 the South China and adjoining seas, *Pure Appl. Geophys.*, 168(6–7), 1153–1173, 2011.
- 690 Paris, R., Switzer, A. D., Belousova, M., Belousov, A., Ontowirjo, B., Whelley, P. L. and
691 Ulvrova, M.: Volcanic tsunami: a review of source mechanisms, past events and hazards in



- 692 Southeast Asia (Indonesia, Philippines, Papua New Guinea), *Nat. Hazards*, 70(1), 447–470,
693 doi:10.1007/s11069-013-0822-8, 2014.
- 694 Park, J.-O., Tsuru, T., Kodaira, S., Cummins, P. R. and Kaneda, Y.: Splay Fault Branching Along
695 the Nankai Subduction Zone, *Science* (80-.), 297(5584), 1157–1160,
696 doi:10.1126/science.1074111, 2002.
- 697 Pautot, G. and Rangin, C.: Subduction of the South China Sea axial ridge below Luzon
698 (Philippines), *Earth Planet. Sci. Lett.*, 92(1), 57–69, doi:[https://doi.org/10.1016/0012-](https://doi.org/10.1016/0012-821X(89)90020-4)
699 [821X\(89\)90020-4](https://doi.org/10.1016/0012-821X(89)90020-4), 1989.
- 700 Peng, D., Hill, E. M., Li, L., Switzer, A. D. and Larson, K. M.: Application of GNSS
701 interferometric reflectometry for detecting storm surges, *GPS Solut.*, 23(2), 47,
702 doi:10.1007/s10291-019-0838-y, 2019.
- 703 Philip, L.-F.: Numerical solutions of three-dimensional run-up on a circular island, *Int.*
704 *Symp. waves-physical Numer. Model. Univ. Br. Columbia, Vancouver Canada, 1994* [online]
705 Available from: <https://ci.nii.ac.jp/naid/10016695852/en/>, 1994.
- 706 Plafker, G.: Tectonic Deformation Associated with the 1964 Alaska Earthquake, *Science* 80,
707 148(3678), 1675–1687, doi:10.1126/science.148.3678.1675, 1965.
- 708 Pollitz, F. F., Brooks, B., Tong, X., Bevis, M. G., Foster, J. H., Bürgmann, R., Smalley Jr., R.,
709 Vigny, C., Socquet, A., Ruegg, J.-C., Campos, J., Barrientos, S., Parra, H., Soto, J. C. B., Cimbaro,
710 S. and Blanco, M.: Coseismic slip distribution of the February 27, 2010 Mw 8.8 Maule, Chile
711 earthquake, *Geophys. Res. Lett.*, 38(9), doi:10.1029/2011GL047065, 2011.
- 712 Power, W., Wallace, L., Wang, X. and Reyners, M.: Tsunami Hazard Posed to New Zealand by
713 the Kermadec and Southern New Hebrides Subduction Margins: An Assessment Based on
714 Plate Boundary Kinematics, Interseismic Coupling, and Historical Seismicity, *Pure Appl.*
715 *Geophys.*, 169(1), 1–36, doi:10.1007/s00024-011-0299-x, 2012.
- 716 Qiu, Q., Hill, E. M., Barbot, S., Hubbard, J., Feng, W., Lindsey, E. O., Feng, L., Dai, K., Samsonov,
717 S. V and Tapponnier, P.: The mechanism of partial rupture of a locked megathrust: The role
718 of fault morphology, *Geology*, doi:10.1130/G38178.1, 2016.
- 719 Ramos, N. T., Maxwell, K. V., Tsutsumi, H., Chou, Y. C., Duan, F., Shen, C. C. and Satake, K.:
720 Occurrence of 1 ka-old corals on an uplifted reef terrace in west Luzon, Philippines:
721 Implications for a prehistoric extreme wave event in the South China Sea region, *Geosci.*
722 *Lett.*, doi:10.1186/s40562-017-0078-3, 2017.
- 723 Ruff, L. and Kanamori, H.: Seismicity and the subduction process, *Phys. Earth Planet. Inter.*,



- 724 23(3), 240–252, doi:10.1016/0031-9201(80)90117-X, 1980.
- 725 Ruff, L. and Kanamori, H.: Seismic coupling and uncoupling at subduction zones,
726 Tectonophysics, 99(2), 99–117, doi:[https://doi.org/10.1016/0040-1951\(83\)90097-5](https://doi.org/10.1016/0040-1951(83)90097-5),
727 1983.
- 728 Ruiz, S., Metois, M., Fuenzalida, A., Ruiz, J., Leyton, F., Grandin, R., Vigny, C., Madariaga, R.
729 and Campos, J.: Intense foreshocks and a slow slip event preceded the 2014 Iquique Mw 8.1
730 earthquake, *Sci.*, 345(6201), 1165–1169, doi:10.1126/science.1256074, 2014.
- 731 Salman, R., Hill, E. M., Feng, L., Lindsey, E. O., Mele vedu, D., Barbot, S., Banerjee, P.,
732 Hermawan, I. and Natawidjaja, D. H.: Piecemeal Rupture of the Mentawai Patch, Sumatra:
733 The 2008 Mw7.2 North Pagai Earthquake Sequence, *J. Geophys. Res. Solid Earth*, (Figure 1),
734 1–16, doi:10.1002/2017JB014341, 2017.
- 735 Satake, K. and Atwater, B. F.: Long-Term Perspectives on Giant Earthquakes and Tsunamis
736 at Subduction Zones, *Annu. Rev. Earth Planet. Sci.*, 35(1), 349–374,
737 doi:10.1146/annurev.earth.35.031306.140302, 2007.
- 738 Schellart, W. P. and Rawlinson, N.: Global correlations between maximum magnitudes of
739 subduction zone interface thrust earthquakes and physical parameters of subduction
740 zones, *Phys. Earth Planet. Inter.*, doi:10.1016/j.pepi.2013.10.001, 2013.
- 741 Schurr, B., Asch, G., Hainzl, S., Bedford, J., Hoechner, A., Palo, M., Wang, R., Moreno, M.,
742 Bartsch, M., Zhang, Y., Oncken, O., Tilmann, F., Dahm, T., Victor, P., Barrientos, S. and Vilotte,
743 J.-P.: Gradual unlocking of plate boundary controlled initiation of the 2014 Iquique
744 earthquake, *Nature*, doi:10.1038/nature13681, 2014.
- 745 Sella, G. F., Dixon, T. H. and Mao, A.: REVEL: A model for Recent plate velocities from space
746 geodesy, *J. Geophys. Res. Solid Earth*, 107(B4), ETG 11-1-ETG 11-30,
747 doi:10.1029/2000JB000033, 2002.
- 748 Singh, S. C., Hananto, N., Mukti, M., Robinson, D. P., Das, S., Chauhan, A., Carton, H., Gratacos,
749 B., Midnet, S., Djajadihardja, Y. and Harjono, H.: Aseismic zone and earthquake
750 segmentation associated with a deep subducted seamount in Sumatra, *Nat. Geosci.*, 4(5),
751 308–311 [online] Available from: <http://www.nature.com/doi/10.1038/ngeo1119>
752 (Accessed 30 August 2011), 2011.
- 753 Song, T. R. A. and Simons, M.: Large trench-parallel gravity variations predict seismogenic
754 behavior in subduction zones, *Science* 80, doi:10.1126/science.1085557, 2003.
- 755 Stevens, V. L. and Avouac, J.: Interseismic Coupling on the Main Himalayan Thrust, *Geophys.*



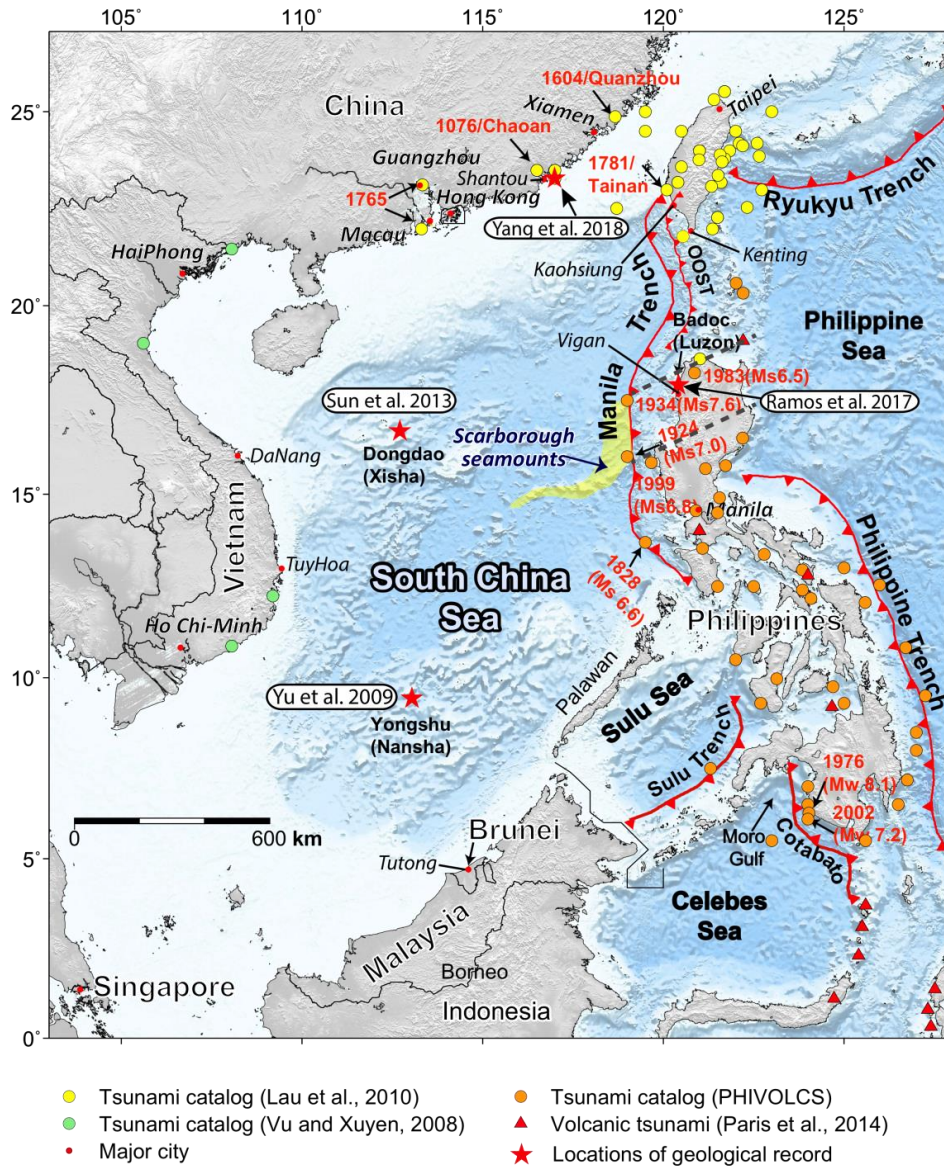
- 756 Res. Lett., n/a-n/a, doi:10.1002/2015GL064845, 2015.
- 757 Sun, L., Zhou, X., Huang, W., Liu, X., Yan, H., Xie, Z., Wu, Z., Zhao, S., Shao, D. and Yang, W.:
- 758 Preliminary evidence for a 1000-year-old tsunami in the South China Sea, *Sci. Rep.*, 3, 1655,
- 759 doi:10.1038/srep01655, 2013.
- 760 Suppe, J.: Tectonics of arc-continent collision on both sides of the South China Sea: Taiwan
- 761 and Mindoro, *Acta Geol. Taiwanica*, (26), 1–18, 1988.
- 762 Taylor, B. and Hayes, D. E.: The Tectonic Evolution of the South China Basin, in *The Tectonic*
- 763 *and Geologic Evolution of Southeast Asian Seas and Islands*, pp. 89–104, American
- 764 Geophysical Union (AGU), 2013.
- 765 Terry, J. P., Winspear, N., Goff, J. and Tan, P. H. H.: Past and potential tsunami sources in the
- 766 South China Sea: A brief synthesis, *Earth-Science Rev.*, 167, 47–61,
- 767 doi:<https://doi.org/10.1016/j.earscirev.2017.02.007>, 2017.
- 768 Vigny, C., Simons, W. J. F., Abu, S., Bamphenyu, R., Satirapod, C., Choosakul, N., Subarya, C.,
- 769 Socquet, a, Omar, K., Abidin, H. Z. and Ambrosius, B. a C.: Insight into the 2004 Sumatra-
- 770 Andaman earthquake from GPS measurements in southeast Asia., *Nature*, 436(7048), 201–
- 771 6, doi:10.1038/nature03937, 2005.
- 772 Vigny, C., Socquet, A., Peyrat, S., Ruegg, J.-C., Métois, M., Madariaga, R., Morvan, S., Lancieri,
- 773 M., Lacassin, R., Campos, J., Carrizo, D., Bejar-Pizarro, M., Barrientos, S., Armijo, R., Aranda,
- 774 C., Valderas-Bermejo, M.-C., Ortega, I., Bondoux, F., Baize, S., Lyon-Caen, H., Pavez, A., Vilotte,
- 775 J. P., Bevis, M., Brooks, B., Smalley, R., Parra, H., Baez, J.-C., Blanco, M., Cimbaro, S. and
- 776 Kendrick, E.: The 2010 Mw 8.8 Maule Megathrust Earthquake of Central Chile, Monitored
- 777 by GPS, *Science* 80, 332(6036), 1417–1421, doi:10.1126/science.1204132, 2011.
- 778 Wang, K.: Elastic and viscoelastic models of crustal deformation in subduction earthquake
- 779 cycles, *Seism. Zo. subduction thrust faults*, 540–575, 2007.
- 780 Wang, K. and Bilek, S. L.: Do subducting seamounts generate or stop large earthquakes?,
- 781 *Geology*, 39(9), 819–822, doi:10.1130/G31856.1, 2011.
- 782 Wang, X., Liu, P. L.-F. and Orfila, A.: NUMERICAL SIMULATIONS OF TSUNAMI RUNUP ONTO
- 783 A THREE-DIMENSIONAL BEACH WITH SHALLOW WATER EQUATIONS, in *Advanced*
- 784 *Numerical Models for Simulating Tsunami Waves and Runup*, pp. 249–253., 2008.
- 785 Wei, S., Graves, R., Helmberger, D., Avouac, J.-P. and Jiang, J.: Sources of shaking and flooding
- 786 during the Tohoku-Oki earthquake: A mixture of rupture styles, *Earth Planet. Sci. Lett.*,
- 787 333–334, 91–100, doi:<http://dx.doi.org/10.1016/j.epsl.2012.04.006>, 2012.



- 788 Wells, R. E., Blakely, R. J., Sugiyama, Y., Scholl, D. W. and Dinterman, P. A.: Basin-centered
789 asperities in great subduction zone earthquakes: A link between slip, subsidence, and
790 subduction erosion?, *J. Geophys. Res. Solid Earth*, 108(B10), doi:10.1029/2002JB002072,
791 n.d.
- 792 Wesnousky, S. G.: Seismological and structural evolution of strike-slip faults, *Nature*,
793 335(6188), 340–343 [online] Available from: <http://dx.doi.org/10.1038/335340a0>, 1988.
- 794 Wesnousky, S. G.: Predicting the endpoints of earthquake ruptures, *Nature*, 444(7117),
795 358–360 [online] Available from: <http://dx.doi.org/10.1038/nature05275>, 2006.
- 796 Wu, J., Suppe, J., Lu, R. and Kanda, R.: Philippine Sea and East Asian plate tectonics since 52
797 Ma constrained by new subducted slab reconstruction methods, *J. Geophys. Res. Solid*
798 *Earth*, 121(6), 4670–4741, doi:10.1002/2016JB012923, 2016.
- 799 Wu, T.-R. and Huang, H.-C.: Modeling tsunami hazards from Manila trench to Taiwan, *J.*
800 *Asian Earth Sci.*, 36(1), 21–28, doi:10.1016/j.jseaes.2008.12.006, 2009.
- 801 Xie, X., Chen, C., Li, L., Wu, S., Yuen, D. A. and Wang, D.: Tsunami hazard assessment for atoll
802 islands inside the South China Sea: A case study of the Xisha Archipelago, *Phys. Earth*
803 *Planet. Inter.*, 290, 20–35, doi:<https://doi.org/10.1016/j.pepi.2019.03.003>, 2019.
- 804 Yang, W., Sun, L., Yang, Z., Gao, S., Gao, Y., Shao, D., Mei, Y., Zang, J., Wang, Y. and Xie, Z.:
805 Nan’ao, an archaeological site of Song dynasty destroyed by tsunami, *Chinese Sci. Bull.*,
806 64(1), 107–120, 2018.
- 807 Yokota, Y., Ishikawa, T., Watanabe, S., Tashiro, T. and Asada, A.: Seafloor geodetic
808 constraints on interplate coupling of the Nankai Trough megathrust zone, *Nature*,
809 534(7607), doi:10.1038/nature17632, 2016.
- 810 Yu, H., Liu, Y., Yang, H. and Ning, J.: Modeling earthquake sequences along the Manila
811 subduction zone: Effects of three-dimensional fault geometry, *Tectonophysics*, 733, 73–84,
812 doi:<https://doi.org/10.1016/j.tecto.2018.01.025>, 2018.
- 813 Yu, K.-F., Zhao, J.-X., Shi, Q. and Meng, Q.-S.: Reconstruction of storm/tsunami records over
814 the last 4000 years using transported coral blocks and lagoon sediments in the southern
815 South China Sea, *Quat. Int.*, 195(1), 128–137,
816 doi:<https://doi.org/10.1016/j.quaint.2008.05.004>, 2009.
- 817 Zhu, J., Sun, Z., Kopp, H., Qiu, X., Xu, H., Li, S. and Zhan, W.: Segmentation of the Manila
818 subduction system from migrated multichannel seismics and wedge taper analysis, *Mar.*
819 *Geophys. Res.*, doi:10.1007/s11001-013-9175-7, 2013.



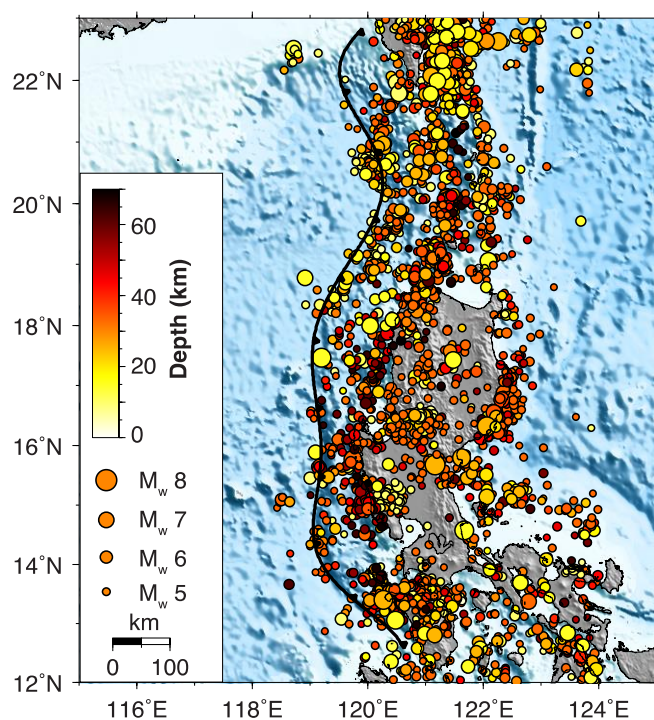
820
 821
 822 **Figures**



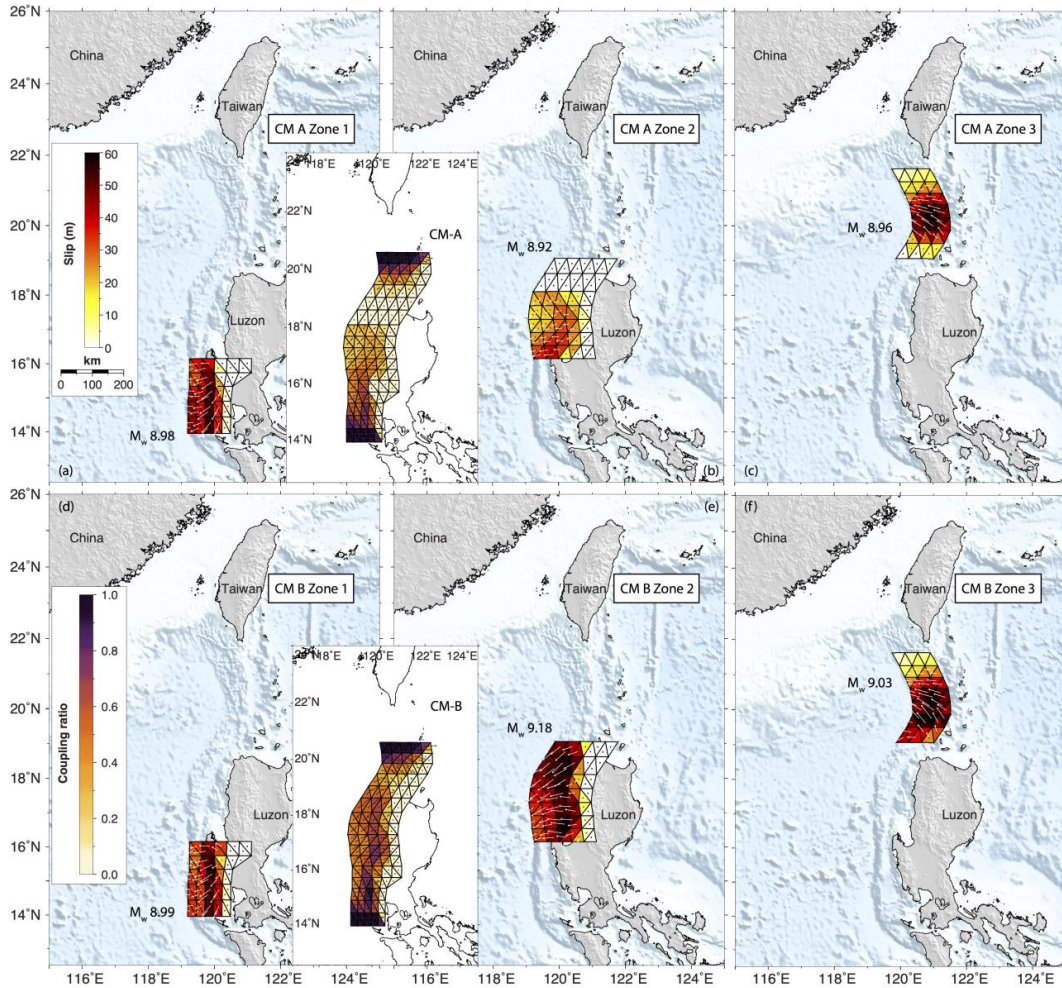
823
 824 **Figure 1.** Tectonic setting and historical tsunami catalogs in the South China Sea region.
 825 Colored circles indicate published tsunami catalogs and are labeled in the legend. Red
 826 triangles represent historical tsunamis related to volcanic activities. Red barbed curves
 827 show the megathrusts in this region. Geological tsunami records are marked with red stars
 828 (Ramos et al., 2017; Sun et al., 2013; Yang et al., 2018; Yu et al., 2009). The megacities are
 829 labeled in the legend and the seafloor subducting features are highlighted in the map. The
 830 historical earthquakes with $M_w > 6.5$ in Philippines are labeled. The likely tsunami events
 831 reported in the mega-cities are also labeled in the map. The two dashed lines represent the



832 possible trace of the subducted Scarborough seamounts underneath the overriding plate as
833 imaged from tomography study (Wu et al., 2016).
834

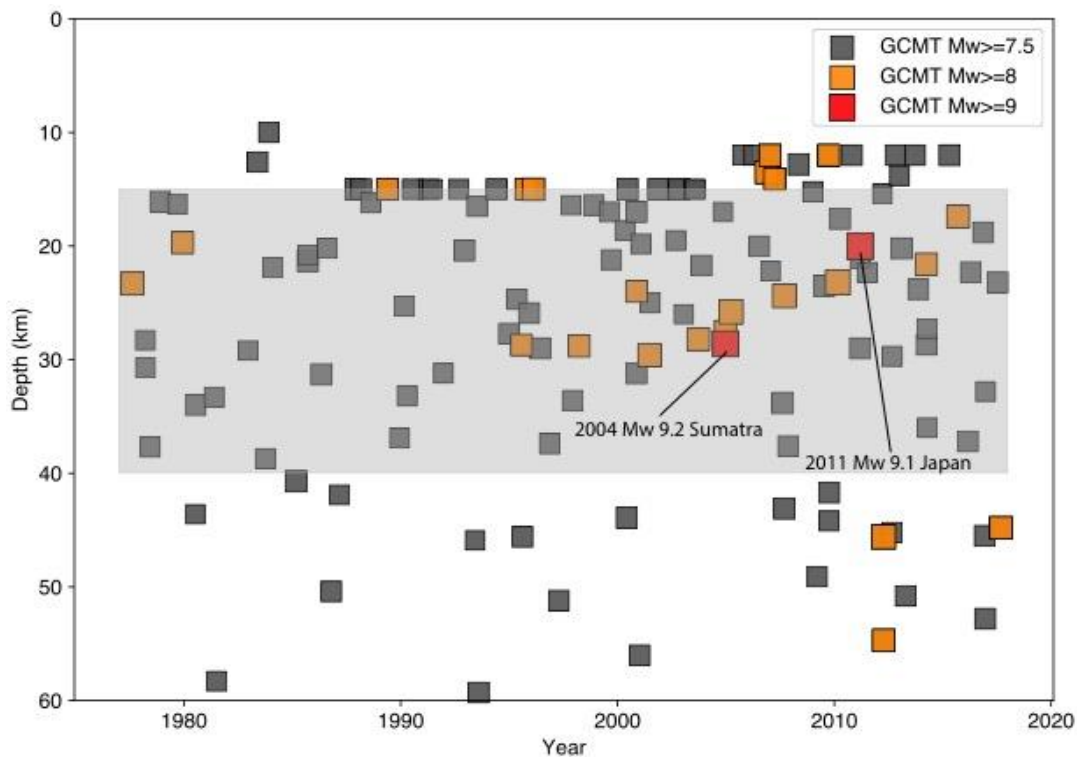


835
836
837 **Figure 2.** Seismicity ($M_w > 4.5$) in the Manila subduction zone between 1900 and 2018.
838 This data set is downloaded from USGS catalog. Color represents the depth and size scales
839 the seismic moment magnitude indicated in the legend.
840



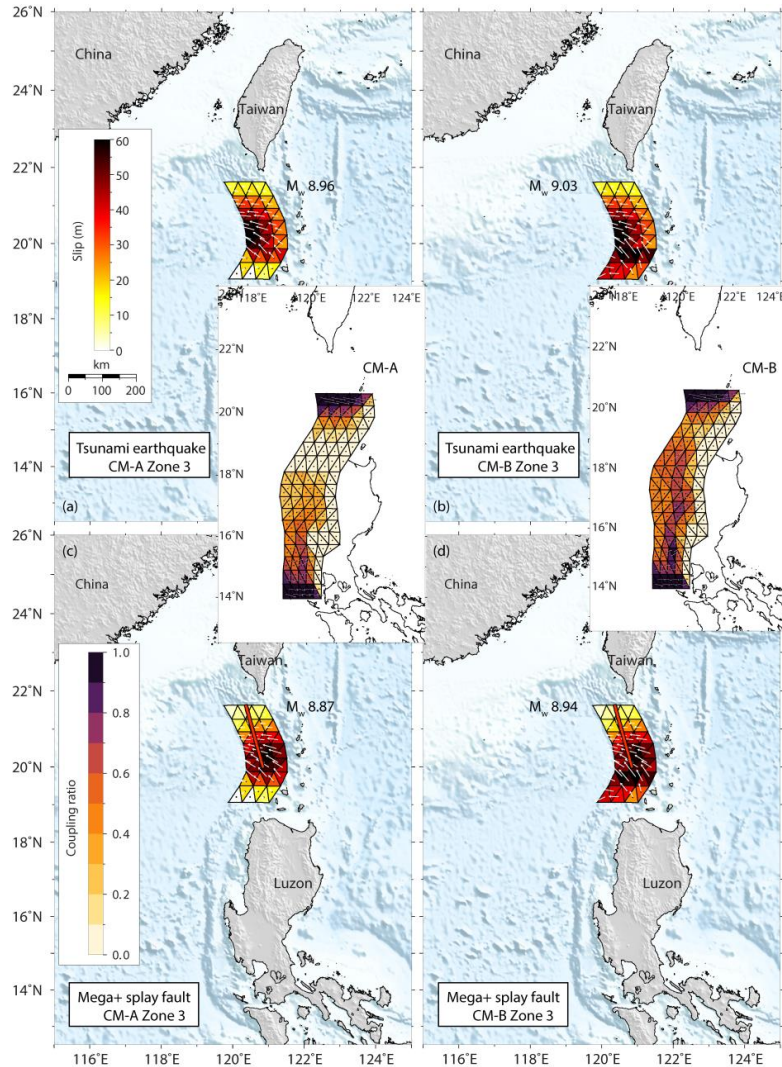
841
 842

843 **Figure 3.** Proposed rupture slip models based on coupling models from Hsu et al. (2016)
 844 assuming a 1000-year seismic return time period. (a) and (b) show the slip models from
 845 coupling model A (Hsu et al., 2016) in zone 1 and 2, respectively. (c) shows a proposed
 846 hybrid model based on coupling model A (19 °N to 20 °N) and a Gaussian shape of slip
 847 distribution (20 °N to 21.7 °N) with 50% coupling ratio in zone 3. (d), (e) and (f) represent
 848 the same slip models with (a), (b) and (c) but based on coupling model B (Hsu et al., 2016).
 849 CM refers to coupling model. Coupling models A and B are from Hsu et al. (2016) that are
 850 shown in the inset map. White arrows show the possible slip directions during earthquake.
 851 Vectors in the coupling maps show the slip deficit direction that is accumulated for future
 852 release in earthquakes. The estimated seismic moment of each model are labeled in each
 853 subplot with rigidity 30 GPa. The slip magnitude and coupling ratio are shown by its
 854 corresponding color scales.



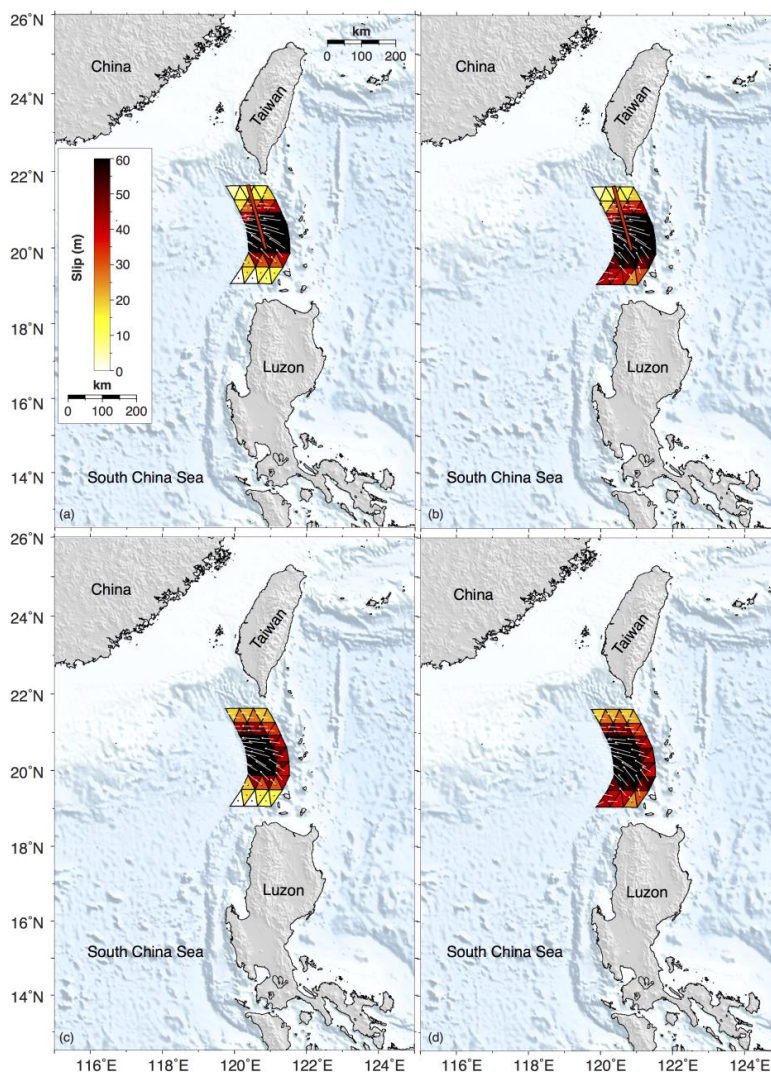
855
856
857
858
859
860

Figure 4. Depth distribution of the seismicity in the Manila subduction zone between 1970 and 2018. This data set is downloaded from GCMT catalog. Colors represent the seismic moment magnitude. The giant 2004 Sumatra and 2011 Japan earthquakes are highlighted in the map.



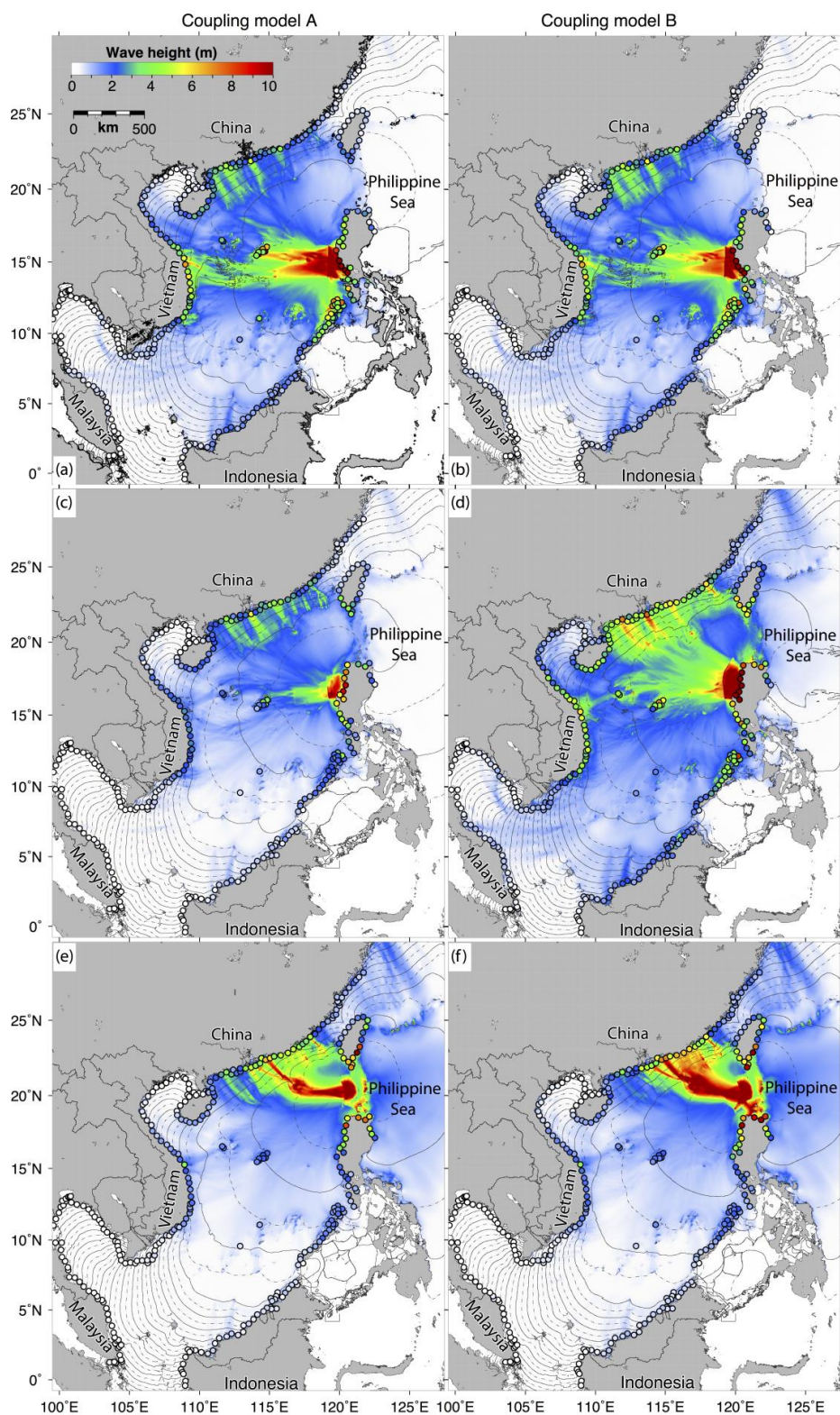
861
862
863
864
865
866
867
868
869
870
871

Figure 5. Proposed slip models in zone 3. (a) and (b) show shallow rupture type of slip models (e.g., Tokoku-Oki) based on coupling models A and B (Hsu et al., 2016), respectively. (c) and (d) represent megathrust (Figure 3. c and f) rupture together with the out-of-sequence megasplay type of slip models, respectively. We assume 50% coupling for the megathrust and the megasplay faults. CM refers to coupling model shown in the inset map. White arrows show the possible slip directions during earthquakes. Vectors in the coupling maps show the slip deficit direction that is accumulated for future release in earthquakes.



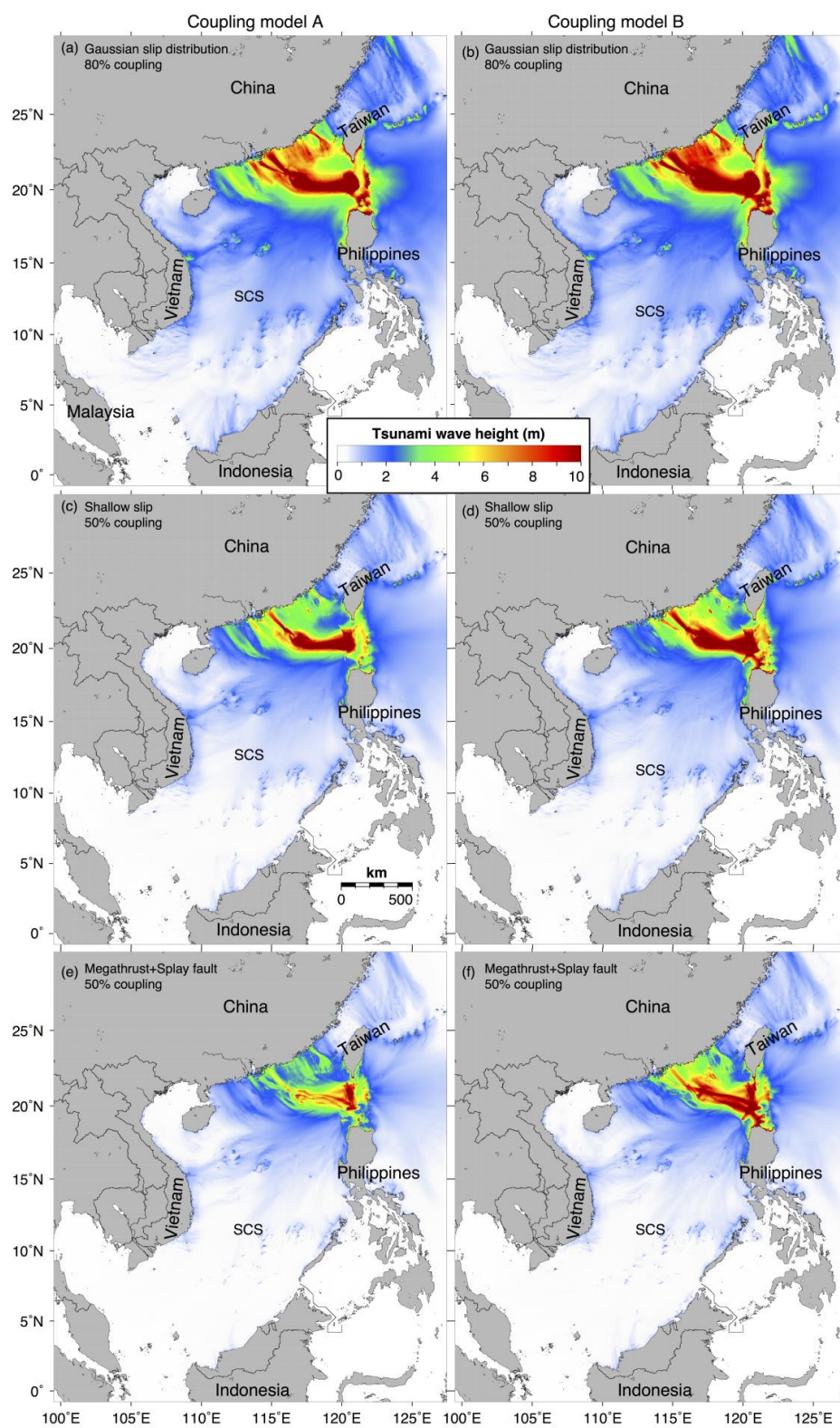
872
873
874
875
876
877
878
879

Figure 6. (a) Seismogenic megathrust rupture together with mega-splay rupture scenario with 80% coupling ratio on each of them from model A of Hsu et al. (2016). (b) same with (a) but from model B of Hsu et al. (2016). (c) Shallow rupture (e.g., Tohoku-Oki rupture) the same as Figure 3.a but with 80% coupling ratio on the megathrust. (d) Shallow rupture (e.g., Tohoku-Oki rupture) same as Figure 3.b but with 80% coupling ratio on the megathrust. A 1000-year seismic return period was assumed in the slip calculation.



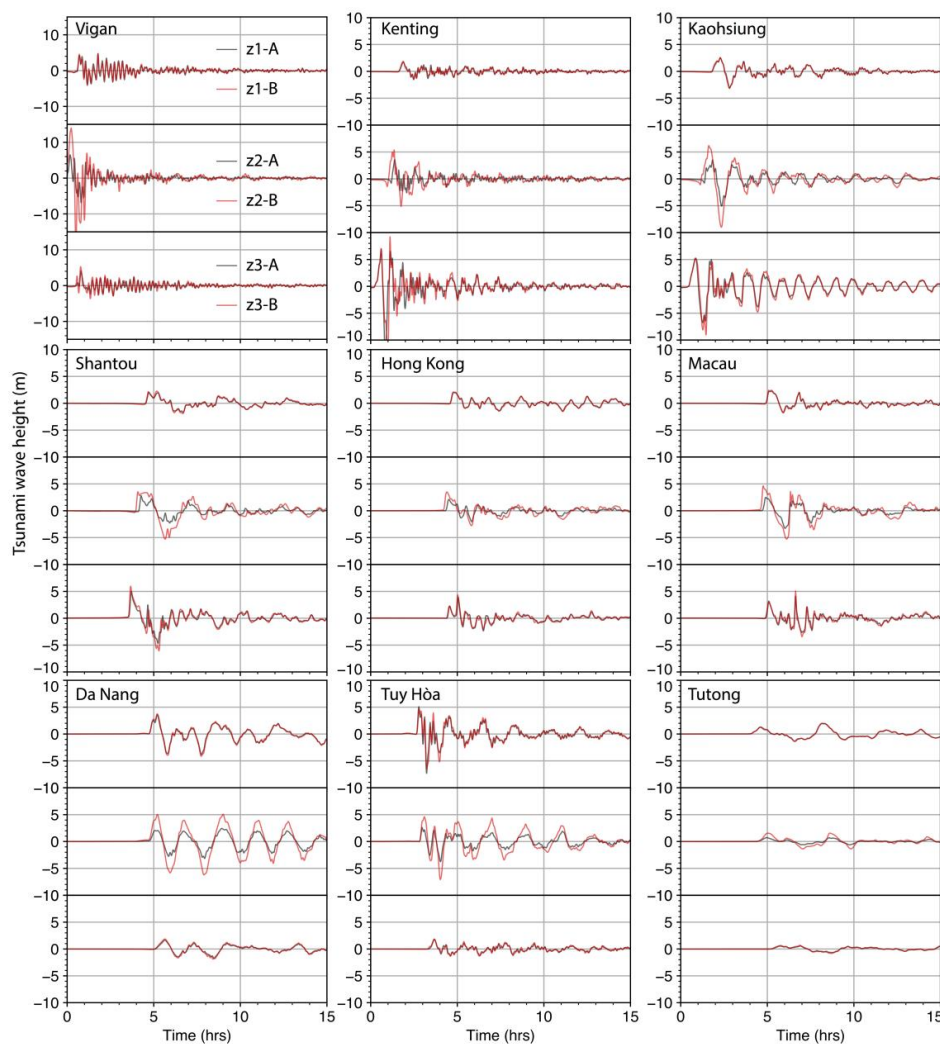


881
882 **Figure 7.** Modeled maximum tsunami wave heights and arrival time contours in SCS. (a),
883 (c) and (e) show the maximum tsunami wave heights generated from rupture zones 1, 2
884 and 3 based on slip models calculated from coupling model A (Hsu et al., 2016),
885 respectively. (b), (d) and (f) show the same maximum tsunami wave heights but with slip
886 models calculated from coupling model B (Hsu et al., 2016). In zone 3, we show Gaussian
887 slip distribution with 50% coupling ratio scenario with other example scenarios shown in
888 Figure 8. The solid black contours show hourly tsunami arrival time with half an hour
889 increment (dashed contours). The colored dots show the subsampled location at 20-m
890 water depth, with color showing the maximum wave heights.





892 **Figure 8.** Maximum tsunami wave heights from different rupture characteristics in zone 3
893 with hybrid coupling models. (a), (c) and (e) show the maximum tsunami wave heights
894 based on coupling model A (Hsu et al., 2016). (b), (d) and (f) show the same maximum
895 tsunami wave heights but with slip models based on coupling model B (Hsu et al., 2016).
896
897



898 **Figure 9.** Simulated tsunami wave time histories at example coastal cities in the SCS region.
899 Top panel, middle and bottom of each subpanel show simulated waves from ruptures in
900 zones 1, 2 and 3, respectively. A and B represent coupling models A and B from Hsu et al.
901 (2016). For rupture zone 3, we show the Gaussian slip distribution with 50% coupling ratio
902 cases (Figure 3. c and f) as examples.
903